Size Matters: Altering the Metal-Surface Coordination in Micropores via Structural Confinement Effects

Journal:	*Inorganic Chemistry Frontiers*
Manuscript ID	QI-RES-05-2024-001261.R2
Article Type:	Research Article
Date Submitted by the Author:	27-Aug-2024
Complete List of Authors:	Southern, Scott; Ames National Laboratory, Chemical and Biological Sciences Thompson, Austin; Iowa State University, Chemistry Sadow, Aaron; Iowa State University, Department of Chemistry Perras, Frédéric; Ames Laboratory, Chemical and Biological Sciences

SCHOLARONE™
Manuscripts

ARTICLE

Size Matters: Altering the Metal-Surface Coordination in Micropores via Structural Confinement Effects

Scott A. Southern,[a] Austin Thompson, [b] Aaron D. Sadow,[a,b] and Frédéric A. Perras *[a,b]

Solid-state NMR experiments were used to investigate the dynamics of supported complexes grafted to a series of silica gel materials of varied pore sizes. Through dipolar recoupling measurements, we found that ligand dynamics were impeded in the more confined environments, as would be expected. A new form of motion involving the complex as a whole, however, appeared in the most restricted environment consisting of 22 Å diameter pores. These motions persisted down to -100 °C at which point the ligands were frozen on the NMR timescale. The newly observed dynamics could only result from the breaking of secondary dative metal-siloxane interactions that otherwise lock the complex in a preferred orientation on the surface. Crucially, these results show that confinement effects alone can be sufficient to reduce a grafted metal's effective coordination number in direct analogy to the synthesis of undercoordinated complexes using bulky ligands. This finding could have important implications in the synthesis of more active heterogeneous catalysts.

Introduction

Dynamics plays a crucial, albeit poorly understood, role in catalysis. For instance, rapid structural rearrangements can produce short-lived species dominating catalysis while also enabling the on-the-fly dynamic stabilization of transition states.[1–6] Despite this, there have not been significant attempts at purposefully modulating the dynamics of single-site heterogeneous complexes, at least partly due to the challenges associated with quantifying the motions. Structural features such as support surface curvature can generate conformational changes[7] that alter how molecular species arrange themselves within pores and likely also how they move. It is thus of interest to determine if and how confinement could be leveraged to control the equilibrium dynamics of supported complexes.

Confinement effects are already known to occasionally have outsized effects on catalysis,[8–15] which can also show nonlinear behavior. Specifically, optimal pore geometries can sometimes be identified in certain reactions.[11] To date, it has been challenging to isolate the root cause of the changes to catalysis observed under confinement;[16–18] however, evidence suggests that the curvature of the pore does have important steric contributions.[19,20] Notable examples of these steric effects include the higher stereoselectivity typically observed in supported Ziegler-Natta olefin polymerization catalysts,[21–26] the increases in polymer molecular weights produced by confined polymerization catalysts[27–30] due to a relative disfavoring of β-alkyl elimination,[31] and the higher enantioselectivities obtained

from supported single-site catalysts.[32–43] These steric effects undoubtedly include a dynamic contribution.
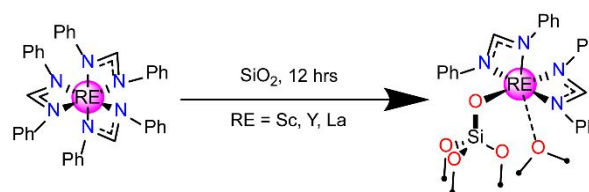
Scheme 1. Representation of the grafting procedure of the rare earth formamidate complexes to silica gel.

Solid-state nuclear magnetic resonance (NMR) spectroscopy has shown great promise in studying equilibrium dynamics in supported metal complexes.[44–48] The gold standard for measuring molecular motions in solids is ^{2}H lineshape analysis,[49–52] which has been used to great success in surface-supported sites.[53–61] ^{1}H-^{13}C dipolar coupling tensors provide analogous information with a much-improved chemical resolution and have further found some use in the study of motions in supported metal complexes.[45,47,62–65] Aside from these methods, ^{13}C chemical shift anisotropy (CSA),[45,46] ^{45}Sc quadrupolar coupling,[66] and ^{1}H CSA[48] have also been applied for this purpose.

Herein, we applied variable temperature (VT) ^{1}H-^{13}C dipolar coupling measurements to investigate how the motions of supported rare earth (RE=Sc, Y, La) formamidate complexes (see **Scheme 1**) are impacted by steric interactions with the silica gel support. Formamidate ligands were chosen for this purpose as they enable the independent measurement of rotations about the surface from the internal motions of the ligands, which are conveniently resolved via ^{13}C detection. Previous work involving supported carbene complexes has suggested that higher-Z metal complexes tended to display greater levels of dynamics,

and it is interesting to determine whether this trend is preserved in other systems.[45]

Experimental

Synthetic Details

General. All manipulations were conducted under an inert atmosphere on a Schlenk line or in a nitrogen filled glovebox unless otherwise mentioned. Triethyl orthoformate (formyl-^{13}C, 99%) and aniline (^{13}C$_6$, 99%) were obtained from Cambridge Isotope Laboratories and used as received. Anhydrous LaCl$_3$, ScCl$_3$, and YCl$_3$ were obtained from Strem Chemicals and used as received. Sc{(NiPr)$_2$CH}$_3$ was obtained from Strem and sublimed before use. Davisil silica materials (Sigma-Aldrich) were calcined at 500 °C under air for 12 h (ramp rate 2 °C/min), partially dehydroxylated under dynamic vacuum at 550 °C for 12 h (ramp rate 2 °C/min) and stored in an N$_2$-filled glovebox. The silanol content in the silica materials was measured by NMR titration using the protonation of Bn$_2$Mg to form toluene in benzene-d_6 with Si(SiMe$_3$)$_4$ as an internal standard of known concentration (Table S1).

N,N'-Bis(phenyl)formamidine-^{13}C$_{13}$. The preparation is modified from the reported ligand synthesis to use ^{13}C-enriched aniline and triethylorthoformate.[67] Enriched aniline-^{13}C$_6$ (0.211 g, 2.13 mmol, 0.37 equiv.) and unenriched aniline (0.885 g, 9.50 mmol, 1.63 equiv.) were loaded into a 100 mL storage tube equipped with a gas-tight, resealable Teflon valve. Triethyl orthoformate-^{13}C (0.868 g, 5.82 mmol, 1 equiv.) was then added, followed by one drop of glacial acetic acid. The storage tube was sealed under nitrogen and heated to 130 °C in an oil bath for 17 h. The reaction mixture was allowed to cool to room temperature, at which point it solidified. The reaction vessel was opened, pentane was added (10 mL), and the solids were broken up with a spatula. The solids were filtered in air, washed with cold pentane (3 × 10 mL), and dried in $vacuo$ to yield 0.754 g (64.9 %) of N,N'-Bis(phenyl)formamidine-^{13}C$_{13}$ as a tan solid, which was enriched with ^{13}C$_6$-Ph to 22% by mass and used without further purification. ^{1}H NMR (600 MHz, chloroform-d): δ 8.19 (d, $^1J_{CH}$ = 174 Hz, 1 H, formyl ^{13}CH), 7.31 (t, $^1J_{CH}$ = 154 Hz (satellite), $^3J_{HH}$ = 7.8 Hz, 4 H, $meta$-C$_6$H$_5$), 7.08 (t, overlapping satellite, $^3J_{HH}$ = 7.2 Hz, 2 H, $para$-C$_6$H$_5$), 7.05 (d, $^1J_{CH}$ = 152 Hz (satellite), $^3J_{HH}$ = 7.8 Hz, 4 H, $ortho$-C$_6$H$_5$). ^{13}C{^{1}H} NMR (151 MHz, chloroform-d): δ 148.74 (br, formyl ^{13}CH), 145.20 (t, $^1J_{CC}$ = 59.3 Hz, $ipso$-C$_6$H$_5$), 129.54 (vtd, $^1J_{CC}$ = 57.7 Hz, $^3J_{CC}$ = 8.6 Hz, $meta$-C$_6$H$_5$), 123.5 (tdt, $^1J_{CC}$ = 55.9 Hz, $^3J_{CC}$ = 10.7 Hz, $^2J_{CC}$ = 3.0 Hz, $para$-C$_6$H$_5$), 119.05 (br vt, $^1J_{CC}$ = 76 Hz, $ortho$-C$_6$H$_5$).

Potassium N,N'-bis(phenyl)formamidate-^{13}C$_{13}$ (K[(NPh)$_2$CH-^{13}C$_{13}$]). K[(NPh)$_2$CH-^{13}C$_{13}$] was synthesized by a modified literature procedure.[68] N,N'-Bis(phenyl)formamidine-^{13}C$_{13}$ (0.153 g, 0.767 mmol, 1 equiv.) was dissolved in anhydrous THF (8 mL). Potassium hydride (0.040 g, 0.998 mmol, 1.3 equiv.) was added in small portions to the stirring solution, resulting in effervescence and a mild exotherm. After complete addition, the solution was allowed to stir for 4 h. The suspension was filtered through a 0.45 μm glass fiber filter, and the volatiles were removed in $vacuo$. The solid residue was washed with

pentane (3 × 5 mL) and dried in $vacuo$ to yield K[(NPh)$_2$CH-^{13}C$_{13}$] (0.180 g, 99%) as an off-yellow solid which was used without further purification. ^{1}H NMR (600 MHz, benzene-d_6): δ 8.80 (dt, $^1J_{CH}$ = 154.2 Hz, 3 Hz, 1 H, formyl ^{13}CH), 7.31 (t, $^1J_{CH}$ = 154 Hz (satellite),$^3J_{HH}$ = 9 Hz, 4 H, $meta$-C$_6$H$_5$), 6.97-6.94 (m, 6 H, $ortho/para$-C$_6$H$_5$). ^{13}C{^{1}H} NMR (151 MHz, benzene-d_6): δ 162.3 (s, formyl ^{13}CH), 154.9 (td, $^1J_{CC}$ = 60.4 Hz, $^3J_{CC}$ = 7.5 Hz, $ipso$), 129.8 (td, $^1J_{CC}$ = 55.9 Hz, $^3J_{CC}$ = 7.6 Hz, $meta$), 120.4 (bt, $^1J_{CC}$ = 62 Hz, overlapping $ortho/para$).

Scandium tris[N,N'-bis(phenyl-^{13}C$_6$)formamidate] (Sc{κ^2-(NPh)$_2$CH-^{13}C$_{13}$}$_3$). Sc{κ^2-(NPh)$_2$CH}$_3$ was previously reported by Faden et al. from reaction of PhN=CH–NHPh and metallic Sc nanoparticles and characterized by single crystal X-ray diffraction.[69] ScCl$_3$ (0.025 g 0.168 mmol, 1 equiv.) was suspended in anhydrous THF (8 mL) and stirred vigorously. A THF solution of K[(NPh)$_2$CH-^{13}C$_{13}$] (0.120 g, 0.505 mmol, 3 equiv.) was added in a dropwise fashion to the stirring suspension. The reaction mixture became increasingly turbid as it was stirred for 12 h. The solution was filtered through a 0.45 μm glass fibre filter, and the solvent removed in $vacuo$. The residue was lyophilized by dissolving in benzene (5 mL), freezing the solution, and subliming the benzene in $vacuo$ to yield Sc{κ^2-(NPh)$_2$CH-^{13}C$_{13}$}$_3$ (0.091 g, 85.0%) as a pale-yellow solid, which was used without further purification. ^{1}H NMR (400 MHz, benzene-d_6): δ 7.82 (d, $^1J_{CH}$ = 174 Hz, 3 H, formyl ^{13}CH), 7.10 (m, $^1J_{CH}$ = 154 Hz (satellite), 12 H, $meta$-C$_6$H$_5$), 6.91 (m, 18 H, $ortho/para$-C$_6$H$_5$). ^{13}C{^{1}H} NMR (100.62 MHz, benzene-d_6): δ 149.6 (br, formyl ^{13}CH), 146.1 (t, $^1J_{CC}$ = 60.2 Hz, $ipso$-C$_6$H$_5$), 129.5 (vt, J = 55.6 Hz, $meta$-C$_6$H$_5$), 123.4 (vt, J = 53.6 Hz, $para$-C$_6$H$_5$), 120.0 (vt, J = 58.3 Hz, $ortho$-C$_6$H$_5$).

Immobilization of rare earth formamidates onto silica supports. Davisil-type silica was suspended in anhydrous benzene (5 mL) and the suspension was gently stirred. Excess rare earth tris(formamidate) (1.5 equiv. relative to mmol of silanols on the silica) dissolved in benzene (2 mL) was added dropwise to the stirring suspension. The suspension was allowed to stir for 12 h. The supernatant was then carefully decanted, and the silica washed with benzene (4 × 5 mL). The solid was dried in $vacuo$ to furnish a colorless material. Solid-state NMR spectroscopy was used to characterize the ^{13}C-labelled grafted materials. Unenriched rare-earth formamidates were grafted onto silica supports in an analogous manner. The loadings of the rare-earth formamidate complexes on the supports were determined by performing the grafting reactions in NMR tubes to measure the consumption of the precursor from solution and the formation of free amidine (**Table S2**). N$_2$ physisorption measurements were performed to confirm that the ligands were grafting inside the pores of the supports (**Table S3**).

Solid-State NMR Spectroscopy

Solid-state NMR dipolar coupling experiments were conducted using either an Agilent DD2 400 MHz spectrometer equipped with an Agilent 3.2 mm T3 HFXY magic angle spinning (MAS) probe or a Bruker Avance Neo 600 MHz spectrometer equipped with either 4 mm or 2.5 mm triple resonance MAS probes operating in double-resonance mode.

VT $^{13}C\{^1H\}$ phase-alternating *R*-symmetry (PARS)[70,71] or proton-detected local-field (PDLF)[65,72,73] experiments (pulse sequences are shown in **Figure S1a** and **b**) were carried out at 9.4 T, with temperatures ranging from -100 °C to room temperature. In an argon glovebox, the samples were center-packed in 3.2 mm pencil-style rotors and spun at 11.111 kHz under a flow of nitrogen gas. The w$R18_2^5$ recoupling sequence[74] was applied to ^1H nuclei using a 50% window duration and 100 kHz radiofrequency (RF) power. The rotor-synchronized t_1 recoupling period was incremented in 24-32 steps, with 64-256 scans acquired for each spectrum, depending on the sensitivity. Cross-polarization (CP) to ^{13}C was applied using a ^1H tangent contact pulse with a contact time lasting 2 ms for PARS and 0.15 ms for PDLF. In all cases, the recycle delay was set to 2 s. The observed dipolar evolution is cosine-modulated in relation to the recoupling time and is best represented using a cosine transformation.[75] **Figure S2** describes the simple procedure used to obtain the cosine-transformed spectra.

Two-dimensional *γ*-free ^1H triple-quantum single-quantum (TQ/SQ) correlation experiments[76] were carried out on a using either a Bruker Avance III 600 MHz spectrometer equipped with an Agilent 1.6 mm T3 HXY MAS probe or an Agilent DD2 400 MHz spectrometer equipped with a 1.8 mm Samoson double resonance probe. The pulse sequence is shown in **Figure S1c**. The samples were packed in an argon glovebox and then spun to 40 kHz under a flow of nitrogen gas. Experimental parameters were first calibrated using tyrosine HCl, and then recalibrated for each sample to achieve 100 kHz ^1H RF power.

Density Functional Theory

Density functional theory (DFT) calculations were performed using the Amsterdam Density Functional (ADF) program.[77] Geometry optimizations were executed at the PBE/TZP level of theory with the basis set increased to TZ2P+ for Sc.[78] Optimizations incorporated Grimme's D3 dispersion correction.[79–81] Relativistic effects were included using the scalar zeroth order relativistic approximation (ZORA).[82–84]

Theory

Nuclear spins interact through a distance-dependent direct dipolar spin-spin coupling interaction. The strength of the interaction is quantified by the dipolar coupling constant (*D*), described as,

$$D = \left(\frac{\mu_0}{4\pi}\right)\left(\frac{\gamma_i\gamma_j}{2\pi}\right)r_{i,j}^{-3} \tag{1}$$

where μ_0 is the vacuum magnetic permeability, γ_n are the gyromagnetic ratios of the coupled spins, and $r_{i,j}$ denotes the internuclear distance between spins indexed as i and j. In a bonded ^1H-^{13}C pair, *D* is approximately 23 kHz.

The spatial dependence of the dipolar coupling interaction, thoroughly detailed in previous studies,[47,48] can be summarized by a few key points. The orientation of the dipolar interaction is described by an axially symmetric tensor, $\mathbf{D}_{PAS}$.

$$\mathbf{D}_{PAS} = D\begin{pmatrix} 0.5 & 0 & 0 \\ 0 & 0.5 & 0 \\ 0 & 0 & -1 \end{pmatrix} \tag{2}$$

This tensor can be rotated into an arbitrary laboratory frame, $\mathbf{D}_{LAB}$, using a set of rotation matrices (**R**). We use the ZYZ convention in this context, where *α*, *β* and *γ* are Euler angles.

$$\mathbf{D}_{LAB} = \mathbf{R}_Z^{-1}(\gamma)\mathbf{R}_Y^{-1}(\beta)\mathbf{R}_Z^{-1}(\alpha)\mathbf{D}_{PAS}\mathbf{R}_Z(\alpha)\mathbf{R}_Y(\beta)\mathbf{R}_Z(\gamma) \tag{3}$$

The Euler angles *α*, *β*, and *γ* are time-dependent in the presence of motions. In the fast-motion limit, the observed dipolar coupling is simply the time average of the matrix, $\langle\mathbf{D}\rangle$

$$\langle\mathbf{D}\rangle = \frac{1}{t}\int_0^t \mathbf{D}_{LAB}\mathrm{d}t \tag{4}$$

which simplified to equation 5 in cases where dynamics can be treated as jumps between *N* discrete molecular orientations.

$$\langle\mathbf{D}\rangle = \frac{1}{N}\sum_{i=1}^N \mathbf{D}_{LAB},i \tag{5}$$

The eigenvalues of $\langle\mathbf{D}\rangle$ are obtained by diagonalisation, where the eigenvalues are ordered as $|\langle D_{33}\rangle| \geq |\langle D_{22}\rangle| \geq |\langle D_{11}\rangle|$. The averaged dipolar coupling constant, $\langle D\rangle$, is equal to $\langle D_{33}\rangle$. Dynamics may further result in a dipolar asymmetry, characterized by the dimensionless asymmetry parameter, $\langle\eta_D\rangle$, which ranges from 0, in axially symmetric cases, to 1.

$$\langle\eta_D\rangle = \frac{\langle D_{11}\rangle - \langle D_{22}\rangle}{\langle D_{33}\rangle} \tag{6}$$

The amplitude of the motions is often characterized by a dimensionless order parameter, $\langle S_D\rangle$, that describes the reduction in the dipolar coupling strength caused by dynamics.

$$\langle S_D\rangle = \frac{\langle D\rangle}{D} \tag{7}$$

A schematic representation of the grafting of tris(N,N'-di-Ph-formamidinato)scandium(III) to silica gel (Sc{κ^2-(NPh)$_2$CH}$_2$/SiO$_2$) is shown in **Scheme 1**. The complexes may feature two distinct dynamic modes, namely, rotations around the N-Ph and Si-O-Sc bonds, which can each be spectroscopically resolved using NMR (**Figure 1a**). Due to local C_2 symmetries, both dynamic modes can be characterized by two-site jump dynamics, i.e. $(\vartheta,\varphi) = (\vartheta, 0°$ and 180°). In this simplified context, we can calculate $\langle S_D\rangle$ directly, which has the following dependence on the angle ϑ.

$$\langle S_D\rangle = \begin{cases} \left(3\cos^2\frac{\theta}{2} - 1\right)\!/2 & \theta = 0° - 70° \\ 0.5 & \theta = 70° - 108° \\ \left(3\sin^2\frac{\theta}{2} - 1\right)\!/2 & \theta = 108° - 180° \end{cases} \tag{8}$$

In the case of a phenyl two-site jump, ϑ=120°, for the *ortho* and *meta* ^{13}C-^1H pairs, and we expect $\langle S_D\rangle$ values of 0.625. Predicting the order parameter for the central formamidate ^{13}C-^1H pairs in the presence of surface reorientation is more challenging. DFT calculations performed on a molecular model predict an H-Sc-H angle of 104° between the two formamidate ligands (see supporting information), while this angle was predicted to range from 90° to 130° in the related
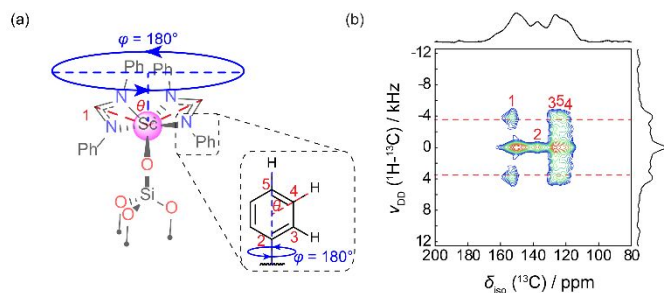
ARTICLE

Figure 1. (a) Possible dynamic modes of supported scandium formamidate complexes. The inset shows the C_2 rotation of Ph moieties. (b) 2D dipolar recoupled PARS spectrum of Sc{κ²-(NPh)$_2$CH}$_2$/SiO$_{2,60Å}$ acquired at -100 °C, with assignments described according to the structure in (a).

Sc{κ²-(NiPr)$_2$CH}$_2$/SiO$_2$ complex using plane-wave DFT,[47] suggesting that $\langle S_D \rangle$ could be reduced to a value ranging from 0.5 to 0.75 if Si-O-Sc motions are present. Note that these motions would also reduce the intra-phenyl $\langle S_D \rangle$ values. In the previously studied Sc{κ²-(NiPr)$_2$CH}$_2$/SiO$_2$ complex, iPr librational dynamics were observed, which required molecular dynamics modelling to predict $\langle S_D \rangle$.[47]

Results

The molecular precursor Sc{κ²-(NPh)$_2$CH}$_3$ was grafted to a variety of Davisil silica gels containing pore diameters of r = 22, 30, 60, and 150 Å, to produce Sc{κ²-(NPh)$_2$CH}$_2$/SiO$_{2,rÅ}$. Shown in **Figure 2a** is a Van der Waals representation of the DFT-optimized cluster model of the complex superimposed on depictions of the four pore geometries.[85] From these models, we estimate that the diameter of the grafted complex (w), accounting for the van der Waal's radii of each atom, is approximately 16.2 Å. The distance between Sc and the surface (d) is approximately 2.9 Å. Geometrically, we can thus estimate that the maximum surface curvature that would allow the complex to bond without significant steric repulsion to be:

$$r = \frac{4d^2 + w^2}{4d} \tag{9}$$

where r is the diameter of the SiO$_2$ pore. Given the DFT-estimated structural parameters, we thus expect that the minimum pore size allowing unhindered bonding to the pore surface is 25 Å. In pores with diameters <25 Å, the complex would need to adopt a distorted structure or weaken its interactions with the support such that it rests closer to the pore center. The effect of the SiO$_2$ curvature is perhaps more clearly illustrated in **Figure 2a** for the specific pore diameters studied here. In particular, the materials with pore diameters 22 Å and 30 Å are likely to result in steric interactions with the complex.

We performed ^{13}C{^{1}H} PARS measurements to gauge the motions of the ligands[86], as described earlier in the Theory section. **Figure 1b** shows the low-temperature 2D PARS spectrum of uniformly ^{13}C-enriched Sc{κ²-(NPh)$_2$CH}$_2$/SiO$_{2,60Å}$ acquired at -100 °C. The resonances between 117 and 137 ppm are assigned to the phenyl ring, while the signal at 155 ppm is

assigned to the central formamidate carbon. The 137 ppm signal does not display any splitting from dipolar interactions, as expected for a quaternary carbon. All other resonances show doublet structures and can be used to measure local order parameters. The values of $\langle S_D \rangle$ for all C-H pairs equal roughly 1.0, suggesting that all motions are frozen at this temperature relative to the timescale of the recoupled dipolar interactions.[87] Slices taken from the indirect dimension of this experiment are also shown in **Figures 2** and **3**.

Figure 2b shows the recoupled ^{13}C-^{1}H dipolar doublets measured for the central amidine carbon resonance as well as the *meta* resonance from the phenyl moieties at temperatures of -100°C and 25 °C for the Sc complexes grafted to each of the four pore sizes. Focusing first on the motions of the entire complex, as seen from the averaging of the dipolar splitting from the amidine ^{13}C-^{1}H spin pair, we first notice that the Sc complexes grafted to 30 and 60 Å supports features $\langle S_D \rangle$ = 1.0 at both low and high temperatures, suggesting they remain strongly bound to the support. In the case of the material supported on the least-hindered support with 150 Å pores, we can see that $\langle S_D \rangle$, first observed to be 1.0 at -100 °C, transforms into a complex multiplet at 25 °C with dominant contributions from doublets with $\langle S_D \rangle$ values of 1.0 and approximately 0.4. A fraction of the complexes supported on this relatively flat surface can thus undergo higher-amplitude motions at room temperature.

Perhaps the strangest case, however, is Sc{κ²-(NPh)$_2$CH}$_2$/SiO$_{2,22Å}$. This material features a central amidine resonance with a ^{13}C-^{1}H $\langle S_D \rangle$ value of approximately 0.9 and 0.8 at room temperature and -100 °C, respectively. This suggests that the complex grafted to the 22 Å pore is destabilized, resulting in increased dynamics, likely due to weakened support-metal bonding.

As expected, room temperature measurements for the phenyl rings show an averaged ^{13}C-^{1}H dipolar coupling resulting in an order parameter $\langle S_D \rangle \approx 0.5$, close to the expected value of 0.6 suggesting that the phenyl ring undergoes fast two-site flipping dynamics with additional averaging due to librational motions. In the case of the 150 Å sample, however, we see a stronger narrowing due to the combined dynamics, which include the rotation of the complex seen using the formamidate resonance. We estimate the order parameter to equal 0.3 at 25 °C, which agrees with the product of the order parameter measured for the formamidate at the same temperature and the value of 0.6 expected from two-fold Ph flips. For the 22 Å sample, we again corroborate the −100°C formamidate $\langle S_D \rangle$ value of 0.9 by seeing a similar averaging in the -100 °C splitting of the *meta* phenyl resonance. Further narrowing is observed at room temperature, in agreement with the addition of two-fold phenyl flips.

As mentioned earlier, the dynamics of d^0 alkylidene and alkylidyne complexes were shown to increase with increasing atomic mass.[45] To determine whether this trend is continued in the rare earths, we repeated the abovementioned measurements on Y{κ²-(NPh)$_2$CH}$_2$/SiO$_{2,60Å}$ and
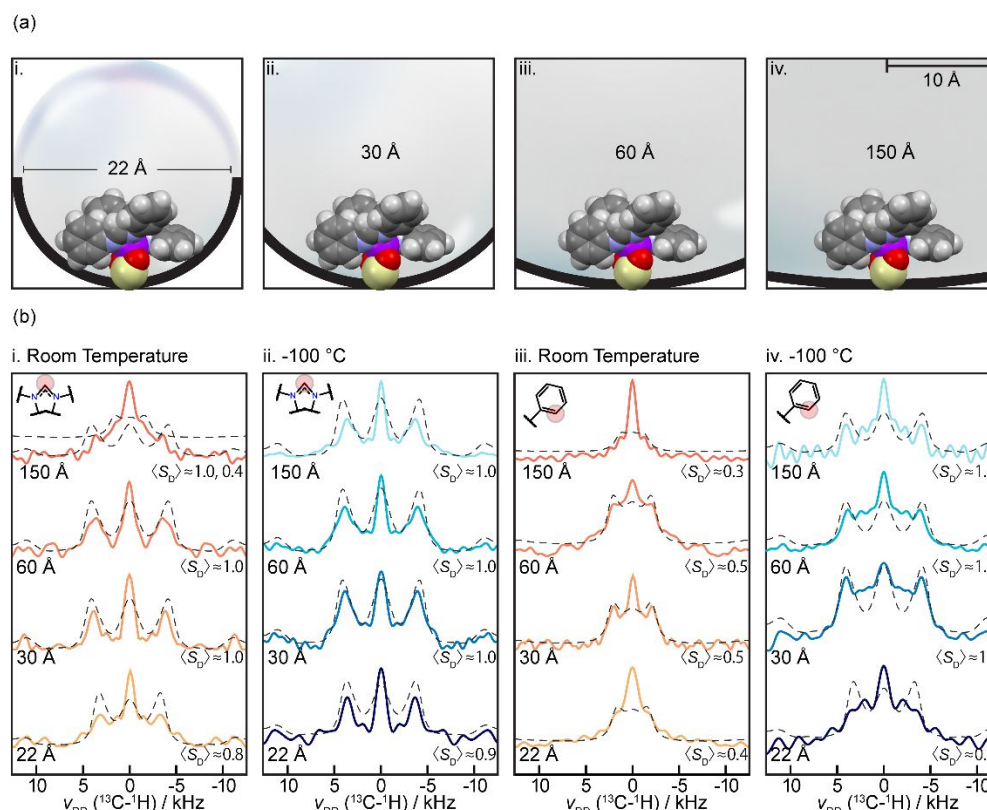
(a)

(b)

Figure 2. (a) Illustration comparing the curvature of the silica gel pore to the overall size of the grafted formamidate complex. The formamidate complex is depicted by the geometry-optimized DFT structure. **(b)** 1D slices from 2D PARS spectra of of Sc{κ^2-(NPh)$_2$CH}$_2$/SiO$_2$ complexes with varying pore sizes (as indicated) were taken at room temperature (i, iii) and -100 °C (ii, iv). SIMPSON[88] simulated dipolar splittings, represented by the black dashed lines, are overlaid onto the data depicted in (b). These simulations used the scaled dipolar coupling corresponding to the indicated order parameter.

La{κ^2-(NPh)$_2$CH}$_2$/SiO$_{2,60Å}$. The observed dipolar splittings from the central formamidate C-H pair are shown in **Figure 3**. In contrast with earlier experiments, we did not observe increased motions, with $\langle S_D \rangle$ remaining close to 1 for all three systems.

Given that the coalescence of the Ph C_2 rotations occurs at a temperature which is accessible to our instruments, unlike the central formamidate CH, we are further able to compare how the barriers for the motions are impacted by confinement. The VT PARS data measured for the *meta* phenyl ^{13}C-^{1}H spin pair are depicted in **Figure 4**. As can be seen, we observed a clear transition from the low-temperature $\langle S_D \rangle$ = 1.0 regime to the high-temperature limit displaying C_2 rotations and a $\langle S_D \rangle$ of roughly 0.6. Lineshapes involving intermediate dynamics simulated using a home-built C++ program that assumes a 2-site hop and employs simple analytic expressions (see supporting information for more details). We were able to obtain high-quality fits to the data and extract phenyl C_2 rotation activation energies of 40.2 ± 0.4, 39 ± 0.5 and 37 ± 0.4 kJ/mol for the complexes supported on the 30, 60 and 150 Å silica gels, respectively. This range of values agrees with some previously determined activation energies measured for similar motions.[89–94] Interestingly, these data also display the intuitive result that motions are impeded in a more restrictive environment. Note that because the metal loading is much lower in Sc{κ^2-(NPh)$_2$CH}$_2$/SiO$_{2,22Å}$, we could not obtain high-quality VT data for this material.
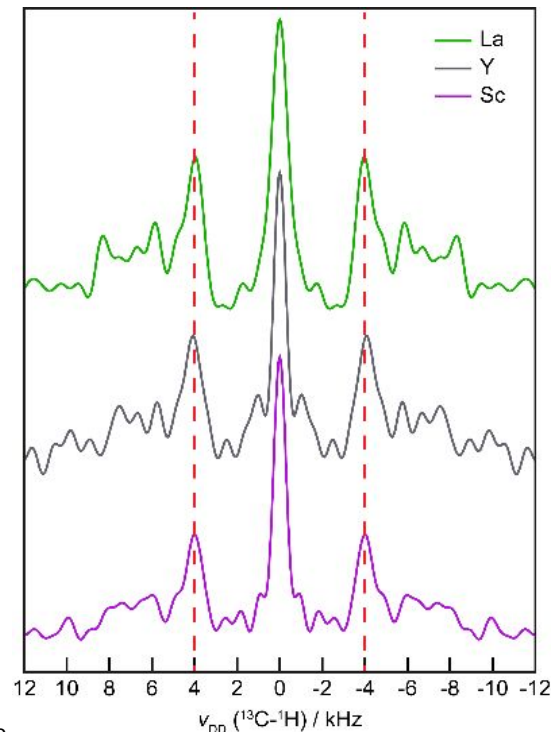
were

Figure 3. Room temperature PDLF dipolar splittings for the central formamidate in RE{κ^2-(NPh)$_2$CH}$_2$/SiO$_{2,60Å}$ (RE: La, Y or Sc). The red dashed line shows that the splittings are unchanged.

ARTICLE
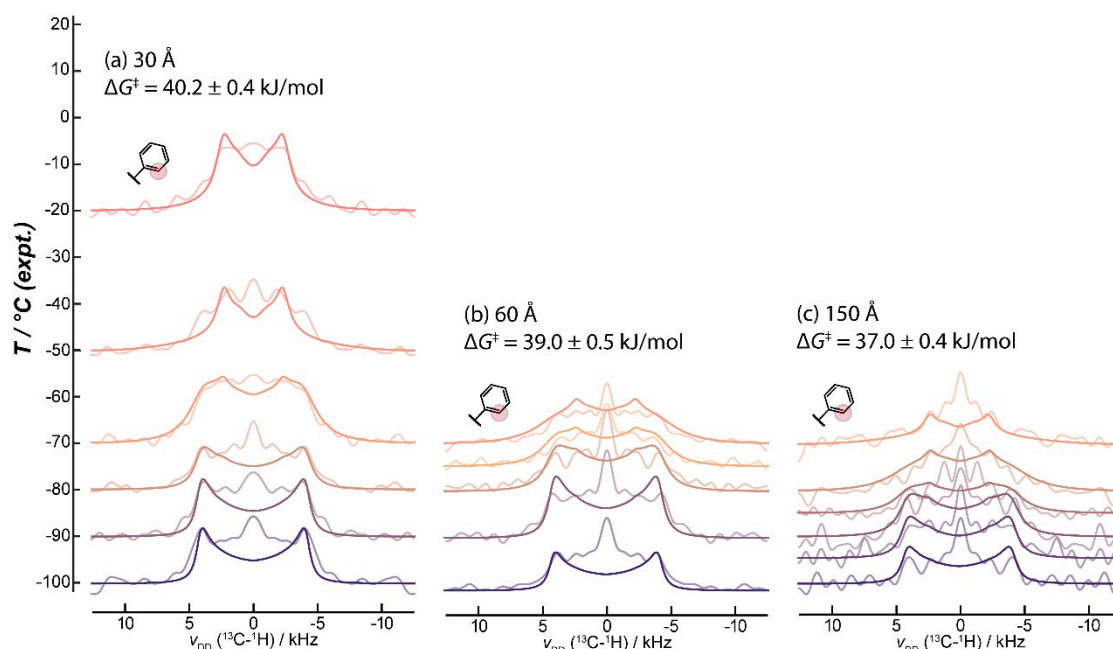
Figure 4. VT PARS data acquired on Sc{κ²-(NPh)₂CH}₂/SiO₂,₃₀Å (a), Sc{κ²-(NPh)₂CH}₂/SiO₂,₆₀Å (b), and Sc{κ²-(NPh)₂CH}₂/SiO₂,₁₅₀Å (c). The bold spectra correspond to the simulated spectra assuming a constant $\Delta G^{\ddagger}$ for each material (see supporting information). The exchange constants were calculated using the Eyring equation. Temperatures are read using the vertical axis and the baseline level of the spectra. Uncertainties were estimated visually by simulation.

Due to sensitivity limitations, all temperature points were simultaneously fit to a single activation energy with exchange rate constants calculated using the Eyring equation. This assumes that the free energy of activation ($\Delta G^{\ddagger}$) is constant in our temperature range, or equivalently, that $T\Delta S^{\ddagger}$ was constant over the narrow temperature range where coalescence is observed.

To rule out whether surface crowding is responsible for the changes in ligand dynamics across our systems,[48,95–97] we attempted to detect intermolecular surface proximities using multiple-quantum spectroscopy. While there are two formamidate ^{1}H sites in each complex which can result in an intramolecular formamidate-formamidate double-quantum coherence, the excitation of a formamidate-only triple-quantum coherence requires the proximity of two complexes.[96,98,99] To efficiently excite the triple-quantum coherences, we applied the 2D γ-free ^{1}H triple-quantum single-quantum (TQ/SQ) correlation experiment.[76] The TQ/SQ correlation spectrum measured for Sc{κ²-(NPh)₂CH}₂/SiO₂,₆₀Å is shown in **Figure 5a**. Unfortunately, due to spectral overlap with the aromatic ^{1}H signals, we could not conclusively rule out clustering in this material. As such, we repeated the experiment on the analogous Sc{κ²-(N*i*Pr)₂CH}₂/SiO₂,₆₀Å complex (**Figure 5b**). The spectrum measured for this latter material is dominated by

intramolecular contacts. We do not observe a formamidate-only TQ correlation from clusters which would be manifested by an autocorrelation signal occurring at approximately 24 ppm in the TQ dimension. These observations suggest that the observed changes of dynamics do not result from intermolecular interactions and are indeed a consequence of confinement.
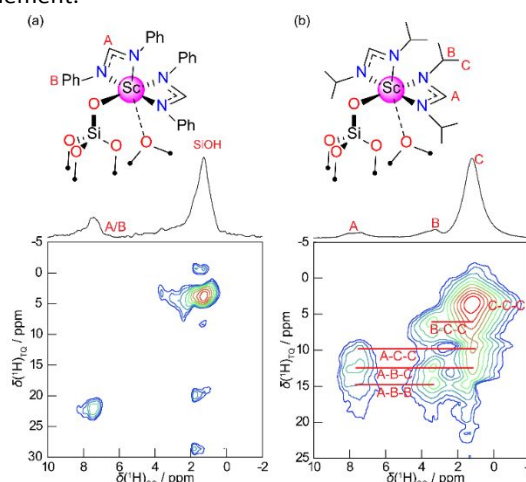

Figure 5. ^{1}H TQ/SQ of (a) Sc{κ²-(N*i*Pr)₂CH}₂/SiO₂,₆₀Å and (b) Sc{κ²-(NPh)₂CH}₂/SiO₂,₆₀Å. Correlations are assigned in accordance with the structures above the spectra.

Discussion

The spatio-dynamic effects seen in Sc{κ^2-(NPh)$_2$CH}$_2$/SiO$_2$ are more complex than was initially expected. As pores sizes are reduced closer to the molecular scale, from 150 to 30 Å, we see a monotonic increase in phenyl rotation barriers from 37 to 41 kJ/mol. This is, of course, expected. As the pore dimensions are reduced, complex-surface steric interactions increase, which is associated with a larger barrier to conformational rearrangement. This is also well exemplified in the complex grafted to 150 Å silica gel, which shows the appearance of secondary rotations of the metal around the surface at higher temperatures. The complexes bound to 30 and 60 Å silica gel only display phenyl rotations, with the complex remaining solidly bound to the surface, as evidenced by the lack of averaging in the central formamidate ^{13}C-^{1}H dipolar coupling.

The most surprising result is the unexpected mobility of Sc{κ^2-(NPh)$_2$CH}$_2$/SiO$_{2,22Å}$. This complex is unique in that the pore dimensions are smaller than would be needed for the complex to comfortably fit in the pores. Unlike the other three complexes, which can be frozen when reducing the sample temperature to -100 °C, this complex undergoes rapid rotations around its Si-O-Sc bonds at all investigated temperatures. This is seen by the averaging of formamidate C-H order parameters to a value of 0.8. This value is in the range expected for a C_2 rotation of the complex but is also distinctly larger than the value of 0.4 measured in Sc{κ^2-(NPh)$_2$CH}$_2$/SiO$_{2,150Å}$ at room temperature, suggesting the potential existence of steric distortions in the complex's coordination environment.

We recently observed the formation of secondary dative interactions between surface siloxane linkages and scandium in a silica-supported scandium borohydride complex.[66] Culver and co-workers also observed similar interactions in a supported scandium metallocene complex.[85] Notably, in the first example, these interactions were absent when the complex was grafted to a zeolitic support, where the complex maintained a high level of mobility.

Based on these literature precedents, we can expect supported rare earth formamidate complexes to also form secondary dative interactions with surface siloxane species. These interactions would impose a substantial barrier to Si-O-Sc rotation as this motion would involve the breaking of a, albeit weak, dative bond. As the pore dimensions are increased, the steric contribution to this barrier is reduced, which enables Sc{κ^2-(NPh)$_2$CH}$_2$/SiO$_{2,150Å}$ to release from the support at room temperature.

Experiments performed on analogous yttrium and lanthanum complexes demonstrated that these interactions remain strong with the softer metals.

As the pore dimensions are reduced to below 25 Å, however, it becomes geometrically impossible for the complex to bend towards the surface and form these sorts of interactions. As such, the Si-O-Sc rotation barrier becomes dominated by the weaker steric contribution, and the complex maintains its mobility down to -100 °C (**Figure 6**). This is a similar result as was seen in Faujasite-supported scandium borohydride.[66]

Importantly, these results highlight a potentially new and valuable structural insight, namely, that highly constrained pore environments may be used to stabilize undercoordinated metal complexes that may be more active in catalysis. This is a direct, heterogeneous, equivalent to the popular use of bulky ligands in molecular inorganic chemistry for the synthesis of undercoordinated metal centers.[100]
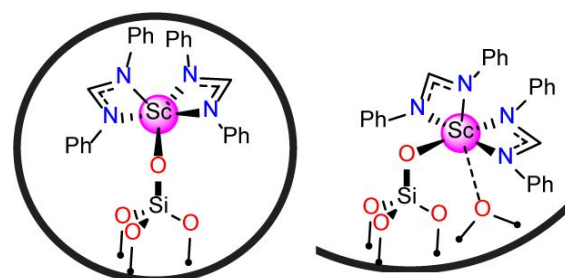

Figure 6. Schematic representation of the pore and coordination environment of Sc{κ^2-(NPh)$_2$CH}$_2$/SiO$_{2,22Å}$ (left) and the other analogues (right).

Conclusions

We have determined several interesting and unique ways in which steric interactions between a metal complex and its support material impact molecular motions and coordination environment. As expected, confined environments impede molecular motions and increase the barriers associated with ligand rearrangement. Highly confined environments can, however, have far more significant impacts.

In pores below the critical diameter to enable comfortable confinement, we observed increased motions. Based on literature precedent, we assigned this change to the steric prevention of secondary dative siloxane metal interactions that otherwise anchor complex's orientation on the support. This observation challenges our conventional understanding of sterics and reveals that confined environments may enable the synthesis of catalytically interesting undercoordinated metals.

Author Contributions

FAP and SAS conceived the presented idea. Catalysts were designed by ADS and AT and synthesized and characterized by SAS and AT. SAS performed NMR experiments and DFT calculations, and SAS and FAP analysed the results.

Data Availability

Additional spectroscopy data (DRIFTS, solution-state NMR, IR) are provided as supplementary information, as are the determined OH and metal loadings of the various materials and their BET data. Supplementary information further contains sample DFT input files and final optimized coordinates, in addition to a detailed description of how the PARS lineshapes were simulated. Raw spectra and program source codes can be obtained from the authors on request.

Conflicts of interest

There are no conflicts to declare.

Acknowledgements

References

1 A. Kohen, Role of Dynamics in Enzyme Catalysis: Substantial versus Semantic Controversies, *Accounts Chem Res*, 2015, **48**, 466–473.

2 H. Zhai and A. N. Alexandrova, Fluxionality of Catalytic Clusters: When It Matters and How to Address It, *Acs Catal*, 2017, **7**, 1905–1911.

3 B. R. Goldsmith, B. Peters, J. K. Johnson, B. C. Gates and S. L. Scott, Beyond Ordered Materials: Understanding Catalytic Sites on Amorphous Solids, *Acs Catal*, 2017, **7**, 7543–7557.

4 H. Zhai and A. N. Alexandrova, Local Fluxionality of Surface-Deposited Cluster Catalysts: The Case of Pt_7 on Al_2O_3, *J Phys Chem Lett*, 2018, **9**, 1696–1702.

5 B. Zandkarimi and A. N. Alexandrova, Dynamics of Subnanometer Pt Clusters Can Break the Scaling Relationships in Catalysis, *J Phys Chem Lett*, 2019, **10**, 460–467.

6 O. Rivoire, Geometry and Flexibility of Optimal Catalysts in a Minimal Elastic Model, *J Phys Chem B*, 2020, **124**, 807–813.

7 M. Peer, A. Qajar, R. Rajagopalan and H. C. Foley, On the effects of confinement within a catalyst consisting of platinum embedded within nanoporous carbon for the hydrogenation of alkenes, *Carbon*, 2014, **66**, 459–466.

8 M. Iwamoto, Y. Tanaka, N. Sawamura and S. Namba, Remarkable Effect of Pore Size on the Catalytic Activity of Mesoporous Silica for the Acetalization of Cyclohexanone with Methanol, *J. Am. Chem. Soc.*, 2003, **125**, 13032–13033.

9 F. Goettmann, D. Grosso, F. Mercier, F. Mathey and C. Sanchez, New P^O ligand grafted on periodically organised mesoporous silicas for one-pot bifunctionnal catalysis: Coupling of base catalysed Knoevenagel condensation with *in situ* Rh catalysed hydrogenation, *Chem. Commun.*, 2004, 1240–1241.

10 F. Goettmann, C. Boissière, D. Grosso, F. Mercier, P. L. Floch and C. Sanchez, New Hybrid Bidentate Ligands as Precursors for Smart Catalysts, *Chem. A Eur. J.*, 2005, **11**, 7416–7426.

11 F. Goettmann and C. Sanchez, How does confinement affect the catalytic activity of mesoporous materials?, *J Mater Chem*, 2006, **17**, 24–30.

12 C. Yu and J. He, Synergic catalytic effects in confined spaces, *Chem. Commun.*, 2012, **48**, 4933–4940.

13 C. C. Gheorghiu, C. S. M. de Lecea and M. C. R. Martínez, Support effects in a Rh diamine complex heterogenized on carbon materials, *ChemCatChem*, 2013, **5**, 1587–1597.

14 J. C. S. Terra, A. R. Martins, F. C. C. Moura, C. C. Weber and A. Moores, Making more with less: confinement effects for more sustainable chemical transformations, *Green Chem.*, 2022, **24**, 1404–1438.

15 M. Tanaka, A. Itadani, Y. Kuroda and M. Iwamoto, Effect of Pore Size and Nickel Content of Ni-MCM-41 on Catalytic Activity for Ethene Dimerization and Local Structures of Nickel Ions, *J. Phys. Chem. C*, 2012, **116**, 5664–5672.

16 W.-H. Chen, S.-J. Huang, Q. Zhao, H.-P. Lin, C.-Y. Mou and S.-B. Liu, On the Confinement Effect During Catalytic Reaction Over Al-MCM-41, *Top. Catal.*, 2008, **52**, 2.

17 E. E. Santiso, M. K. Kostov, A. M. George, M. B. Nardelli and K. E. Gubbins, Confinement effects on chemical reactions-Toward an integrated rational catalyst design, *Appl. Surf. Sci.*, 2007, **253**, 5570–5579.

18 E. E. Santiso, A. M. George, C. H. Turner, M. K. Kostov, K. E. Gubbins, M. Buongiorno-Nardelli and M. Sliwinska-Bartkowiak, Adsorption and catalysis: The effect of confinement on chemical reactions, *Appl. Surf. Sci.*, 2005, **252**, 766–777.

19 S. Pariente, P. Trens, F. Fajula, F. D. Renzo and N. Tanchoux, Heterogeneous catalysis and confinement effects The isomerization of 1-hexene on MCM-41 materials, *Appl. Catal. A: Gen.*, 2006, **307**, 51–57.

20 D. Zhang, W.-Q. Liu, Y.-A. Liu, U. J. Etim, X.-M. Liu and Z.-F. Yan, Pore confinement effect of MoO_3/Al_2O_3 catalyst for deep hydrodesulfurization, *Chem. Eng. J.*, 2017, **330**, 706–717.

21 J. C. W. Chien, J. C. Vizzini and W. Kaminsky, Difference in stereoselective polymerization of 4-methyl-1-hexene by homogeneous and heterogeneous Ziegler-Natta catalysts, *Die Makromol. Chem., Rapid Commun.*, 1992, **13**, 479–484.

22 Y. S. Ko, T. K. Han, J. W. Park and S. I. Woo, Propene polymerization catalyzed over MCM-41 and VPI-5-supported $Et(ind)_2ZrCl_2$ catalysts, *Macromol. Rapid Commun.*, 1996, **17**, 749–758.

23 J. Tudor and D. O'Hare, Stereospecific propene polymerisation catalysis using an organometallic modified mesoporous silicate, *Chem. Commun.*, 1997, 603–604.

24 W. Kaminsky, C. Strübel, H. Lechert, D. Genske and S. I. Woo, Syndiotactic polypropene with MCM-41 supported metallocene [Me₂C(Cp)(Flu)]ZrCl₂, *Macromol. Rapid Commun.*, 2000, **21**, 909–912.

25 C. J. Miller and D. O'Hare, Mesoporous silica-supported zirconocene catalysts for highly isotactic polypropylene, *Chem. Commun.*, 2004, 1710–1711.

26 Y. S. Ko and S. I. Woo, in *Tailor-Made Polymers: Via Immobilization of Alpha-Olefin Polymerization Catalysts*, eds. J. R. Severn and J. C. Chadwick, WILEY-VCH Verlag GmbH & Co. KGaA, Weinheim, 2008, pp. 261–276.

27 W. Kaminsky and F. Renner, High melting polypropenes by silica-supported zirconocene catalysts, *Die Makromol. Chem., Rapid Commun.*, 1993, **14**, 239–243.

28 H. Balcar, J. Sedláček, J. Čejka and J. Vohlídal, MCM-41-Immobilized [Rh(cod)OCH₃]₂ Complex – A Hybrid Catalyst for the Polymerization of Phenylacetylene and Its Ring-Substituted Derivatives, *Macromol. Rapid Commun.*, 2002, **23**, 32–37.

29 C. Alonso-Moreno, D. Pérez-Quintanilla, D. Polo-Cerón, S. Prashar, I. Sierra, I. del Hierro and M. Fajardo, MCM-41/*ansa*-zirconocene supported catalysts: Preparation, characterization and catalytic behaviour in ethylene polymerization, *J. Mol. Catal. A: Chem.*, 2009, **304**, 107–116.

30 H. Xu and C.-Y. Guo, Polymerization in the confinement of molecular sieves: Facile preparation of high performance polyethylene, *Eur. Polym. J.*, 2015, **65**, 15–32.

31 M. E. O'Reilly, S. Dutta and A. S. Veige, β-Alkyl Elimination: Fundamental Principles and Some Applications, *Chem. Rev.*, 2016, **116**, 8105–8145.

32 R. Raja, J. M. Thomas, M. D. Jones, B. F. G. Johnson and D. E. W. Vaughan, Constraining Asymmetric Organometallic Catalysts within Mesoporous Supports Boosts Their Enantioselectivity, *J. Am. Chem. Soc.*, 2003, **125**, 14982–14983.

33 M. D. Jones, R. Raja, J. M. Thomas, B. F. G. Johnson, D. W. Lewis, J. Rouzaud and K. D. M. Harris, Enhancing the

Enantioselectivity of Novel Homogeneous Organometallic Hydrogenation Catalysts, *Angew. Chem. Int. Ed.*, 2003, **42**, 4326–4331.

34 H. Zhang, Y. Zhang and C. Li, Enantioselective epoxidation of unfunctionalized olefins catalyzed by the Mn(salen) catalysts immobilized in the nanopores of mesoporous materials, *J. Catal.*, 2006, **238**, 369–381.

35 K. Malek, A. P. J. Jansen, C. Li and R. A. van Santen, Enantioselectivity of immobilized Mn-salen complexes: A computational study, *J. Catal.*, 2007, **246**, 127–135.

36 J. M. Thomas and R. Raja, Exploiting Nanospace for Asymmetric Catalysis: Confinement of Immobilized, Single-Site Chiral Catalysts Enhances Enantioselectivity, *Acc. Chem. Res.*, 2008, **41**, 708–720.

37 J. M. Fraile, J. I. García, C. I. Herrerías, J. A. Mayoral and E. Pires, Enantioselective catalysis with chiral complexes immobilized on nanostructured supports, *Chem. Soc. Rev.*, 2008, **38**, 695–706.

38 K. D. M. Harris and S. J. M. Thomas, Selected Thoughts on Chiral Crystals, Chiral Surfaces, and Asymmetric Heterogeneous Catalysis, *ChemCatChem*, 2009, **1**, 223–231.

39 Y. Huang, S. Xu and V. S. -Y. Lin, Changing from Symmetric to Asymmetric Simply by Immobilizing the Catalyst on Mesoporous Silica Nanoparticle, *ChemCatChem*, 2011, **3**, 131–134.

40 D. Xia, T. Cheng, W. Xiao, K. Liu, Z. Wang, G. Liu, H. Li and W. Wang, Imidazolium-Based Organic–Inorganic Hybrid Silica as a Functional Platform Dramatically Boosts Chiral Organometallics Performance in Asymmetric Catalysis, *ChemCatChem*, 2013, **5**, 1784–1789.

41 K. K. Bania, G. V. Karunakar, K. Goutham and R. C. Deka, Enantioselective Henry Reaction Catalyzed by "Ship in a Bottle" Complexes, *Inorg. Chem.*, 2013, **52**, 8017–8029.

42 J. M. Fraile, N. García and C. I. Herrerías, Support Effect on Stereoselectivities of Vinylogous Mukaiyama–Michael Reactions Catalyzed by Immobilized Chiral Copper Complexes, *ACS Catal.*, 2013, **3**, 2710–2718.

43 T. Cheng, Q. Zhao, D. Zhang and G. Liu, Transition-metal-functionalized ordered mesoporous silicas: an overview of sustainable chiral catalysts for enantioselective transformations, *Green Chem.*, 2015, **17**, 2100–2122.

44 J. O. Ehresmann, P. W. Kletnieks, A. Liang, V. A. Bhirud, O. P. Bagatchenko, E. J. Lee, M. Klaric, B. C. Gates and J. F. Haw, Evidence from NMR and EXAFS Studies of a Dynamically Uniform Mononuclear Single-Site Zeolite-Supported Rhodium Catalyst, *Angew. Chem. Int. Ed.*, 2006, **45**, 574–576.

45 F. Blanc, J.-M. Basset, C. Copéret, A. Sinha, Z. J. Tonzetich, R. R. Schrock, X. Solans-Monfort, E. Clot, O. Eisenstein, A. Lesage and L. Emsley, Dynamics of Silica-Supported Catalysts Determined by Combining Solid-State NMR Spectroscopy and DFT Calculations, *J. Am. Chem. Soc.*, 2008, **130**, 5886–5900.

46 D. P. Estes, C. P. Gordon, A. Fedorov, W.-C. Liao, H. Ehrhorn, C. Bittner, M. L. Zier, D. Bockfeld, K. W. Chan, O. Eisenstein, C. Raynaud, M. Tamm and C. Copéret, Molecular and Silica-Supported Molybdenum Alkyne Metathesis Catalysts: Influence of Electronics and Dynamics on Activity Revealed by Kinetics, Solid-State NMR, and Chemical Shift Analysis, *J. Am. Chem. Soc.*, 2017, **139**, 17597–17607.

47 A. L. Paterson, D.-J. Liu, U. Kanbur, A. D. Sadow and F. A. Perras, Observing the three-dimensional dynamics of supported metal complexes, *Inorg. Chem. Front.*, 2021, **8**, 1416–1431.

48 S. A. Southern, D. J. Liu, P. Chatterjee, Y. T. Li and F. A. Perras, ^{1}H Chemical Shift Anisotropy: a High Sensitivity Solid-state NMR Dynamics Probe for Surface Studies?, *Phys. Chem. Chem. Phys.*, 2023, **25**, 5348–5360.

49 B. Berglund and J. Tegenfeldt, The determination of quadrupole coupling tensors from single-crystal NMR data, *J Magnetic Reson 1969*, 1978, **30**, 451–455.

50 J. J. Kinnun, A. Leftin and M. F. Brown, Solid-State NMR Spectroscopy for the Physical Chemistry Laboratory, *J Chem Educ*, 2013, **90**, 123–128.

51 P. M. J. Szell, S. Zablotny and D. L. Bryce, Halogen bonding as a supramolecular dynamics catalyst, *Nat Commun*, 2019, **10**, 916.

52 S. S. Gunaga and D. L. Bryce, Modulation of Rotational Dynamics in Halogen-Bonded Cocrystalline Solids, *J. Am. Chem. Soc.*, 2023, **145**, 19005–19017.

53 B. Boddenberg, R. Grosse and U. Breuninger, ^{2}H NMR spectra of trimethylsilyl groups anchored on a silica surface, *Surf Sci Lett*, 1986, **173**, L655–L658.

54 J. A. DiVerdi, T. Kobayashi and G. E. Maciel, Molecular Dynamics of Pyridine Adsorbed on the Silica Surface, *J. Phys. Chem. C*, 2007, **111**, 5982–5989.

55 T. Kobayashi, J. A. DiVerdi and G. E. Maciel, Silica Gel Surface: Molecular Dynamics of Surface Silanols, *J Phys Chem C*, 2008, **112**, 4315–4326.

56 J. Gath, G. L. Hoaston, R. L. Vold, R. Berthoud, C. Copéret, M. Grellier, S. Sabo-Etienne, A. Lesage and L. Emsley, Motional heterogeneity in single-site silica-supported species revealed by deuteron NMR, *Phys Chem Chem Phys*, 2009, **11**, 6962–6971.

57 Q. Wang, E. Jordan and D. F. Shantz, ^{2}H NMR Studies of Simple Organic Groups Covalently Attached to Ordered Mesoporous Silica, *J Phys Chem C*, 2009, **113**, 18142–18151.

58 S. Jayanthi, V. Frydman and S. Vega, Dynamic Deuterium Magic Angle Spinning NMR of a Molecule Grafted at the Inner Surface of a Mesoporous Material, *J Phys Chem B*, 2012, **116**, 10398–10405.

59 A. D. Nicola, A. Correa, S. Bracco, J. Perego, P. Sozzani, A. Comotti and G. Milano, Collective dynamics of molecular rotors in periodic mesoporous organosilica: a combined solid-state 2 H-NMR and molecular dynamics simulation study, *Phys Chem Chem Phys*, 2021, **24**, 666–673.

60 N. B. H. Mares, M. Brodrecht, T. Wissel, S. C. Döller, L. Rösler, H. Breitzke, M. M. Hoffmann, T. Gutmann and G. Buntkowsky, Influence of APTES-Decorated Mesoporous Silica on the Dynamics of Ethylene Glycol Molecules-Insights from Variable Temperature ^{2}H Solid-State NMR, *J. Phys. Chem. C*, 2023, **127**, 19735–19746.

61 E. Steinrücken, T. Wissel, M. Brodrecht, H. Breitzke, J. Regentin, G. Buntkowsky and M. Vogel, ^{2}H NMR study on temperature-dependent water dynamics in amino-acid functionalized silica nanopores, *J. Chem. Phys.*, 2021, **154**, 114702.

62 A. Fechtenkötter, K. Saalwächter, M. A. Harbison, K. Müllen and H. W. Spiess, Highly Ordered Columnar Structures from Hexa-peri-hexabenzocoronenes - Synthesis, X-ray Diffraction, and Solid-State Heteronuclear Multiple-Quantum NMR Investigations, *Angew. Chem. Int. Ed.*, 1999, **38**, 3039–3042.

63 K. Saalwächter, An Investigation of Poly(dimethylsiloxane) Chain Dynamics and Order in Its Inclusion Compound with γ-Cyclodextrin by Fast-MAS Solid-State NMR Spectroscopy, *Macromol. Rapid Commun.*, 2002, **23**, 286–291.

64 M. Wang, M. Bertmer, D. E. Demco and B. Blümich, Segmental and Local Chain Mobilities in Elastomers by ^{13}C–^{1}H Residual Heteronuclear Dipolar Couplings, *J. Phys. Chem. B*, 2004, **108**, 10911–10918.

65 S. V. Dvinskikh, H. Zimmermann, A. Maliniak and D. Sandström, Measurements of motionally averaged heteronuclear dipolar couplings in MAS NMR using R-type recoupling, *J Magn Reson*, 2004, **168**, 194–201.

66 S. A. Southern, Y. Li, D.-J. Liu, A. D. Sadow, L. Qi and F. A. Perras, Enhanced Activity from Coordinatively Unsaturated and Dynamic Zeolite-Bound Organoscandium Species, *ACS Catal.*, 2024, **14**, 9440–9451.

67 K. Hirano, S. Urban, C. Wang and F. Glorius, A Modular Synthesis of Highly Substituted Imidazolium Salts, *Org Lett*, 2009, **11**, 1019–1022.

68 C. M. Zall, L. J. Clouston, V. G. Young, K. Ding, H. J. Kim, D. Zherebetskyy, Y.-S. Chen, E. Bill, L. Gagliardi and C. C. Lu, Mixed-Valent Dicobalt and Iron–Cobalt Complexes with High-Spin Configurations and Short Metal–Metal Bonds, *Inorg. Chem.*, 2013, **52**, 9216–9228.

69 L.-P. Faden, A. Reiß, R. Popescu, C. Donsbach, J. Göttlicher, T. Vitova, D. Gerthsen and C. Feldmann, Sc, Zr, Hf, and Mn Metal Nanoparticles: Reactive Starting Materials for Synthesis Near Room Temperature, *Inorg. Chem.*, 2024, **63**, 1020–1034.

70 X. Lu, H. Zhang, M. Lu, A. J. Vega, G. Hou and T. Polenova, Improving dipolar recoupling for site-specific structural and dynamics studies in biosolids NMR: windowed RN-symmetry sequences, *Phys Chem Chem Phys*, 2016, **18**, 4035–4044.

71 G. Hou, X. Lu, A. J. Vega and T. Polenova, Accurate measurement of heteronuclear dipolar couplings by phase-alternating R-symmetry (PARS) sequences in magic angle spinning NMR spectroscopy, *J Chem Phys*, 2014, **141**, 104202.

72 T. Nakai and T. Terao, Measurements of heteronuclear dipolar powder patterns due only to directly bonded couplings, *Magn. Reson. Chem.*, 1992, **30**, 42–44.

73 A. Gansmüller, J.-P. Simorre and S. Hediger, Windowed R-PDLF recoupling: A flexible and reliable tool to characterize molecular dynamics, *J Magn Reson*, 2013, **234**, 154–164.

74 X. Zhao, J. L. Sudmeier, W. W. Bachovchin and M. H. Levitt, Measurement of NH Bond Lengths by Fast Magic-Angle Spinning Solid-State NMR Spectroscopy: A New Method for the Quantification of Hydrogen Bonds, *J Am Chem Soc*, 2001, **123**, 11097–11098.

75 J. D. van Beek, R. Dupree and M. H. Levitt, Symmetry-based recoupling of ^{17}O–^1H spin pairs in magic-angle spinning NMR, *J. Magn. Reson.*, 2006, **179**, 38–48.

76 Y. Nishiyama, V. Agarwal and R. Zhang, t_1-Noise Suppression by γ-Free Recoupling Sequences in Solid-State NMR for Structural Characterization of Fully Protonated Molecules at Fast MAS, *J Phys Chem C*, 2020, **124**, 26332–26343.

77 G. te Velde, F. M. Bickelhaupt, E. J. Baerends, C. F. Guerra, S. J. A. van Gisbergen, J. G. Snijders and T. Ziegler, Chemistry with ADF, *J. Comput. Chem.*, 2001, **22**, 931–967.

78 E. V. Lenthe and E. J. Baerends, Optimized Slater-type basis sets for the elements 1–118, *J Comput Chem*, 2003, **24**, 1142–1156.

79 M. Ernzerhof and G. E. Scuseria, Assessment of the Perdew–Burke–Ernzerhof exchange-correlation functional, *J. Chem. Phys.*, 1999, **110**, 5029–5036.

80 C. Adamo and V. Barone, Toward reliable density functional methods without adjustable parameters: The PBE0 model, *J. Chem. Phys.*, 1999, **110**, 6158–6170.

81 S. Grimme, J. Antony, S. Ehrlich and H. Krieg, A consistent and accurate ab initio parametrization of density functional dispersion correction (DFT-D) for the 94 elements H-Pu, *J. Chem. Phys.*, 2010, **132**, 154104.

82 E. van Lenthe, E. J. Baerends and J. G. Snijders, Relativistic regular two-component Hamiltonians, *J. Chem. Phys.*, 1993, **99**, 4597–4610.

83 E. van Lenthe, E. J. Baerends and J. G. Snijders, Relativistic total energy using regular approximations, *J. Chem. Phys.*, 1994, **101**, 9783–9792.

84 E. van Lenthe, A. Ehlers and E.-J. Baerends, Geometry optimizations in the zero order regular approximation for relativistic effects, *J. Chem. Phys.*, 1999, **110**, 8943–8953.

85 D. B. Culver, W. Huynh, H. Tafazolian and M. P. Conley, Solid-State ^{45}Sc NMR Studies of Cp*$_2$Sc–OR (R = CMe$_2$CF$_3$, CMe(CF$_3$)$_2$, C(CF$_3$)$_3$, SiPh$_3$) and Relationship to the Structure of Cp*$_2$Sc-Sites Supported on Partially Dehydroxylated Silica, *Organometallics*, 2020, **39**, 1112–1122.

86 S. A. Southern and F. A. Perras, Comparison of methods for the NMR measurement of motionally averaged dipolar couplings, *J. Magn. Reson.*, 2024, **364**, 107710.

87 K. Aebischer, L. M. Becker, P. Schanda and M. Ernst, Evaluating the motional timescales contributing to averaged anisotropic interactions in MAS solid-state NMR, *Magn. Reson.*, 2024, **5**, 69–86.

88 M. Bak, J. T. Rasmussen and N. C. Nielsen, SIMPSON: A General Simulation Program for Solid-State NMR Spectroscopy, *J. Magn. Reson.*, 2000, **147**, 296–330.

89 Z. Dominguez, H. Dang, M. J. Strouse and M. A. Garcia-Garibay, Molecular "Compasses" and "Gyroscopes." III. Dynamics of a Phenylene Rotor and Clathrated Benzene in a Slipping-Gear Crystal Lattice, *J Am Chem Soc*, 2002, **124**, 7719–7727.

90 D. M. Rice, R. J. Wittebort, R. G. Griffin, E. Meirovitch, E. R. Stimson, Y. C. Meinwald, J. H. Freed and H. A. Scheraga, Rotational jumps of the tyrosine side chain in crystalline enkephalin. Hydrogen-2 NMR line shapes for aromatic ring motions in solids, *J. Am. Chem. Soc.*, 1981, **103**, 7707–7710.

91 D. M. Rice, Y. C. Meinwald, H. A. Scheraga and R. G. Griffin, Tyrosyl motion in peptides. Deuterium NMR line shapes and spin-lattice relaxation, *J. Am. Chem. Soc.*, 1987, **109**, 1636–1640.

92 D. A. Ben-efraim and R. Arad-yellin, A dynamic nmr study of restricted rotation of two substituted phenyl groups in a c/s 1,2-diphenylcyclobutane, *Tetrahedron*, 1988, **44**, 6175–6186.

93 N. G. Vassilev and V. S. Dimitrov, Restricted rotation of the phenyl group in β-hydroxyphosphonates: Dynamic NMR and semiempirical studies, *Magn. Reson. Chem.*, 1994, **32**, 639–645.

94 T. Akutagawa and T. Nakamura, Supramolecular approach for solid state Brownian rotators, *Dalton Trans.*, 2008, 6335–6345.

95 T. Kobayashi, I. I. Slowing and M. Pruski, Measuring Long-Range ^{13}C–^{13}C Correlations on a Surface under Natural Abundance Using Dynamic Nuclear Polarization-Enhanced Solid-State Nuclear Magnetic Resonance, *J Phys Chem C*, 2017, **121**, 24687–24691.

96 T. Kobayashi, D. Singappuli-Arachchige, I. I. Slowing and M. Pruski, Spatial distribution of organic functional groups supported on mesoporous silica nanoparticles (2): a study by ^1H triple-quantum fast-MAS solid-state NMR, *Phys Chem Chem Phys*, 2018, **20**, 22203–22209.

97 T. Kobayashi and M. Pruski, Spatial Distribution of Silica-Bound Catalytic Organic Functional Groups Can Now Be Revealed by Conventional and DNP-Enhanced Solid-State NMR Methods, *Acs Catal*, 2019, **9**, 7238–7249.

98 T. Kobayashi, D. Singappuli-Arachchige, Z. Wang, I. I. Slowing and M. Pruski, Spatial distribution of organic functional groups supported on mesoporous silica nanoparticles: a study by conventional and DNP-enhanced ^{29}Si solid-state NMR, *Phys Chem Chem Phys*, 2016, **19**, 1781–1789.

99 S. C. Shekar and F. A. Perras, Multiplex Detection of Multiple-Quantum/Single-Quantum NMR Correlation Spectra, *J. Phys. Chem. C*, 2023, **127**, 7352–7359.

100 L. J. Taylor and D. L. Kays, Low-coordinate first-row transition metal complexes in catalysis and small molecule activation, *Dalton Trans.*, 2019, **48**, 12365–12381.

Additional spectroscopy data (DRIFTS, solution-state NMR, IR) are provided as supplementary information, as are the determined OH and metal loadings of the various materials and their BET data. Supplementary information further contains sample DFT input files and final optimized coordinates, in addition to a detailed description of how the PARS lineshapes were simulated. Raw spectra and program source codes can be obtained from the authors on request.